Supplemental material for: Taming Brillouin optomechanics using supermode microresonators

Min Wang[1,3,*], Zhi-Gang Hu[1,3,*], Chenghao Lao[1,2], Yuanlei Wang[1,2], Xing Jin[2], Xin Zhou[1,3], Yuechen Lei[1,3], Ze Wang[2], Wenjing Liu[2,5], Qi-Fan Yang[2,5,†], and Bei-Bei Li[1,4,‡]

[1]Beijing National Laboratory for Condensed Matter Physics, Institute of Physics, Chinese Academy of Sciences, Beijing 100190, China

[2]State Key Laboratory for Artificial Microstructure and Mesoscopic Physics and Frontiers Science Center for Nano-optoelectronics, School of Physics, Peking University, Beijing 100871, China

[3]University of Chinese Academy of Sciences, Beijing 100049, China

[4]Songshan Lake Materials Laboratory, Dongguan 523808, Guangdong, China

[5]Collaborative Innovation Center of Extreme Optics, Shanxi University, Taiyuan 030006, China

*These authors contributed equally to this work.

† leonardoyoung@pku.edu.cn;

‡ libeibei@iphy.ac.cn

S1. DETAILS FOR SIMULATIONS OF SINGLE-PHOTON OPTOMECHANICAL COUPLING RATE $g_0/2\pi$

To determine the single-photon optomechanical coupling rate of the optical modes and phonon modes for the microresonators, it is essential to obtain the field distributions of both the optical and phonon modes [1]. The field distribution of the optical mode in the microcavity must satisfy the Helmholtz equation [2]:

$$\bigtriangledown \times \bigtriangledown \times \boldsymbol{E}_{\mathbf{j}} = \omega_{0,\mathrm{j}}^2 \mu_0 \epsilon \mathbf{E}_{\mathbf{j}} \tag{S1}$$

where $\omega_{0,\mathrm{j}}$ is the resonance frequency of each optical mode, μ_0 is the vacuum permeability, and ϵ is the isotropic unperturbed spatial permittivity.

The phonon mode is described by the modal equation [2]:

$$\bigtriangledown \cdot (\boldsymbol{c} : \boldsymbol{S}) = -\rho \Omega_{\mathrm{m}}^2 \boldsymbol{u} \tag{S2}$$

where $\boldsymbol{u}$ is the mechanical displacement, $\boldsymbol{c}$ is the stiffness tensor, $\boldsymbol{S} = \bigtriangledown_{\mathrm{s}} \boldsymbol{u}$ is the spatial distribution of the strain tensor, ρ denotes the density, and $\Omega_{\mathrm{m}}/2\pi$ is the resonance frequency of mechanical modes.

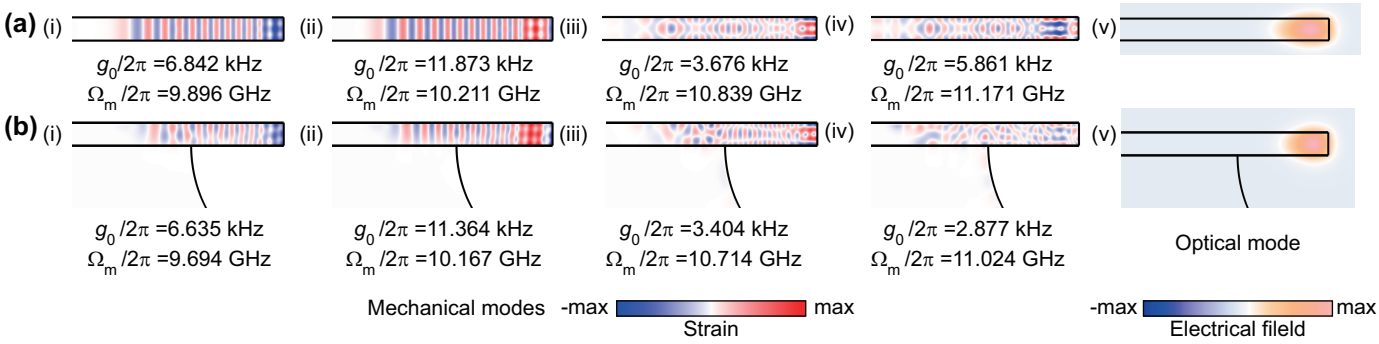

FIG. S1. **Field distributions of the simulated mechanical and optical modes.** (a) and (b) display the results without and with the silicon pedestals. Panels (i-iv) represent the field distributions of the mechanical modes, while (v) illustrates the field distribution of the TE fundamental optical modes.

We employ the finite element method (FEM) simulations to solve Eq. S1 and Eq. S2 to obtain the field distributions of the optical and mechanical modes. Given the symmetry of the SiO_2 microresonators, we utilize cylindrical coordinates (the two-dimensional-axisymmetric model) to construct the geometry of the microresonator. The "Electromagnetic Waves, Frequency Domain" and "Solid Mechanics" modules are utilized to simulate the optical and mechanical modes, respectively. The azimuthal mode numbers of the pump and Stokes modes are set to $m_{\mathrm{p}} = 101$ and

$m_{\mathrm{s}} = -101$, while the azimuthal mode number of the mechanical modes must be $m_a = m_{\mathrm{p}} - m_{\mathrm{s}} = 101 - (-101) = 202$, as dictated by the phase matching condition. We consider only the optical transverse electric (TE) fundamental mode in subsequent calculations, as the mode splitting is supposed to be designed for this mode.

Figure. S1 presents the field distributions of mechanical modes (i-iv) and optical TE fundamental modes (v). The distinction between Figs. S1(a) and S1(b) is whether the silicon pedestals are included in the model. The existence of the silicon pedestal results in reduced confinement of the field distribution for mechanical modes, while the field distribution of the optical modes remains unchanged. Furthermore, the silicon pedestal induces a slight change in the eigenfrequencies of mechanical modes.

In the Brillouin optomechanical interactions in microcavities, the perturbation of the mechanical mode on the optical mode occurs through two effects: the photoelastic effect and the moving boundary effect [1–3]. The total optomechanical coupling rate can be expressed as the sum of these two components, specifically $g_0/2\pi = g_0^{\mathrm{pe}}/2\pi + g_0^{\mathrm{mb}}/2\pi$. The radiation pressure exerted on the surface S of the cavity, with a volume of V, and the unit normal vector $\boldsymbol{n}$ pointing from the inside to the outside of the cavity, together with the spatial distribution of the optical modes for the pump and Stokes (or anti-Stokes) denoted by $\boldsymbol{E}_{\mathbf{p,s}}$, can be used to express these two contributions:

$$g_0^{pe} = -\frac{\omega_{\mathrm{pump}} x_{\mathrm{zpf}}}{2} \int_V \boldsymbol{E}_{\mathbf{p}}^{*} \cdot \delta\boldsymbol{\epsilon}_{\mathrm{pe}} \cdot \boldsymbol{E}_{\mathbf{s}} dV \tag{S3}$$

$$g_0^{mb} = -\frac{\omega_{\mathrm{pump}} x_{\mathrm{zpf}}}{2} \oint_{\mathrm{S}} [\boldsymbol{u} \cdot \boldsymbol{n}][\delta\epsilon_{\mathrm{mb}}[\boldsymbol{E}_{\mathbf{p},//}^{*} \cdot \boldsymbol{E}_{\mathbf{s},//}] - \delta\epsilon_{\mathrm{mb}}^{-1}[\boldsymbol{D}_{\mathbf{p},\perp}^{*} \cdot \boldsymbol{D}_{\mathbf{s},\perp}]] dA \tag{S4}$$

where ω_{pump} is the angular frequency of the pump light, $x_{\mathrm{zpf}} = \sqrt{\frac{\hbar}{2 m_{\mathrm{eff}} \Omega_{\mathrm{m}}}}$ is the zero point fluctuations for a mechanical mode with the angular frequency of Ω_{m} and effective mass of m_{eff}. $\boldsymbol{n}$ denotes the unit normal vector directed from the cavity's interior to its exterior, S and V represent the cavity surface and volume. $\boldsymbol{E}_{\mathbf{p},//}$ and $\boldsymbol{E}_{\mathbf{s},//}$ are the parallel electric fields of the pump and the Stokes (or anti-Stokes) modes, and $\boldsymbol{D}_{\mathbf{p},\perp}$, $\boldsymbol{D}_{\mathbf{s},\perp}$ are the perpendicular electric displacement vectors of the pump and the Stokes (or anti-Stokes) modes, respectively. $\delta\boldsymbol{\epsilon}_{\mathrm{pe}}$ and $\delta\boldsymbol{\epsilon}_{\mathrm{mb}}$ are the permittivity perturbations caused by the photoelastic and moving boundary effects, respectively,

$$\delta\boldsymbol{\epsilon}_{\mathrm{pe}} = -\epsilon_0 n^4 \boldsymbol{p} : \boldsymbol{S} \tag{S5}$$

$$\delta\epsilon_{\mathrm{mb}} = \epsilon_0 (n^2 - n_2^2) \tag{S6}$$

$$\delta\epsilon_{\mathrm{mb}}^{-1} = \epsilon_0^{-1} (n^{-2} - n_2^{-2}) \tag{S7}$$

where ϵ_0 is the vacuum permittivity, $\boldsymbol{p}$ is the photoelastic tensor of the SiO_2, and n_2 is the refractive index outside the cavity. The calculated $g_0/2\pi$ for each mechanical mode is shown in Fig. 2(a) of the main text. The mechanical mode at 10.167 GHz has the highest $g_0/2\pi$=11.364 kHz, which corresponds to a WGM mechanical mode. Figure S2 illustrates that the largest $g_0/2\pi$ approximately scales with $V_{\mathrm{eff}}^{-1/2}$[4], which is expressed as:

$$V_{eff} = \frac{\int |E_p|^2 dV \int |E_S|^2 dV}{\int |E_p|^2 |E_S|^2 dV} \tag{S8}$$

where E_p and E_S denote the electric field intensity of the pump and Stokes fields, respectively. In the case where the pump and Stokes light are in the same spatial modes, the effective mode volume (V_{eff}) is approximately twice the value of the energy-related definition of mode volume [5] ($V_m = \frac{\int |E|^2 dV}{|E_{max}|^2}$), where E_{max} denotes the maximum electric field intensity of the optical mode.

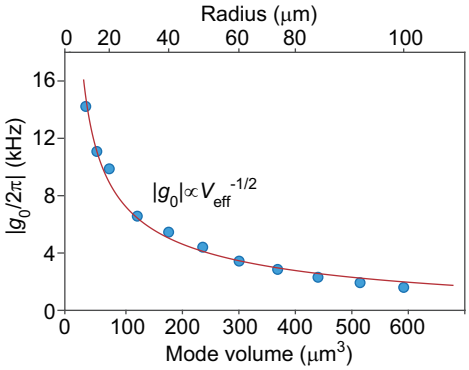

FIG. S2. **Simulated largest $|g_0/2\pi|$ as a function of the radius and mode volume of the microresonator, with the fitting result shown in the red curve.**

S2. DEVICE DESIGN AND CHARACTERIZATION

In this section, we employ the two-dimensional (2D) "Electromagnetic Waves, Frequency Domain" in COMSOL Multiphysics to determine the eigenfrequencies of optical modes of the microresonator with sinusoidally modulated boundaries through FEM simulation. In this 2D approximation, the modes of the infinite cylinders are calculated while constraining the out-of-plane wave number, using the method introduced in Ref. [2]. Specifically, we simulate the eigenfrequencies of SiO_2 microresonators with radii of $r_0 = 15$ μm and 20 μm, and modulation periods of $2m$=148 and 202, respectively, and a thickness of 1 μm. The resulting frequency splitting (Δf) of TE fundamental modes, as a function of the modulation amplitude (α), is plotted in Fig. S3(a). As expected, Δf exhibits a monotonical increase with a growing α and reaches approximately 10 GHz at $\alpha \approx 12$ nm for both cavity sizes. As illustrated in Fig. S3(b), we observe a monotonous increase in Δf with α, which approaches 10 GHz at $\alpha \sim$12 nm for the SiO_2 microresonators with r_0 =15 μm.

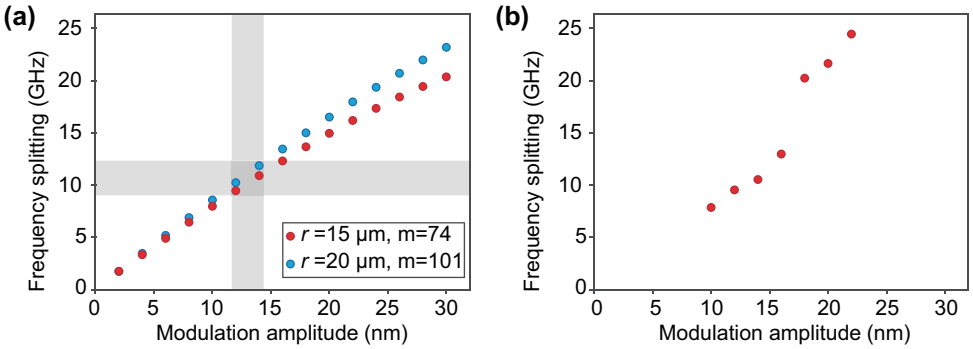

FIG. S3. **Simulated and measured frequency splittings of SiO_2 microresonators.** (a) Simulated frequency splitting (Δf) as a function of the modulation amplitude (α). The gray shaded region indicates the modulation amplitude range of 12-14 nm, which corresponds to a Δf approximately 10 GHz. (b)
Measured frequency splitting (Δf) as a function of the modulation amplitude (α) for SiO_2 microresonators with a radius of $r_0 = 15$ μm.

In the following experiments, the SiO_2 microresonators with r_0 =20 μm are utilized due to their higher optical Q factors. Moreover, during the xenon difluoride etching process, the silicon undercut is maintained at only approximately 5 μm to suppress optomechanical oscillations, which are detrimental to the study of Brillouin optomechanics. Taking into account the fabrication errors, a series of modulations around 12-14 nm for SiO_2 microresonators with a radius of 20 μm are experimentally fabricated. Figure S4(a) presents the measured frequency splitting (Δf) of the SiO_2 microresonators. The measured frequency splittings Δf, ranging from 10-12 GHz, are consistent with the simulated results as α varies from 12.6 nm to 13.8 nm. Owing to the experimentally observed parasitic coupling loss in the system [6], we initially measure the quality factors of the optical modes with relatively weak coupling strength, maintaining the transmission depth on resonance at around 0.9. We then select the optimal cavity for Brillouin optomechanics studies, which has a Δf of 10.404 GHz and Q_0 of 4.3×10^6 and 4.2×10^6 for the higher- and

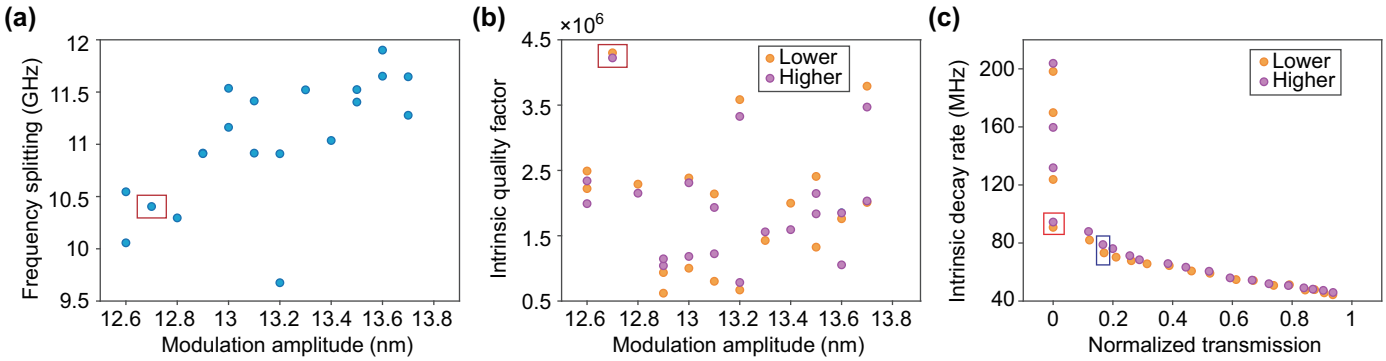

FIG. S4. **Characterization of frequency Splitting and Q Factors of SiO_2 microresonators.** (a) Δf and (b) intrinsic quality factor (Q_0) of the two split modes as a function of the α for SiO_2 microresonators with a radius of $r_0 = 20$ μm, a thickness of $t = 1$ μm, and modulation period of $2m = 202$, respectively. The red box represents the optimal cavity that we used to perform the following two experiments. (c) Intrinsic decay rate ($\kappa_0/2\pi$) for the optimal cavity at different transmission depths on resonance. The orange and purple dots represent the results for the lower- and higher-frequency split modes, respectively. The blue and red boxes correspond to the coupling conditions for the phonon lasing and strong coupling measurements.

lower-frequency split modes, respectively, as denoted by the red box in Fig. S4(b). Figure S4(c) presents the intrinsic decay rates ($\kappa_0/2\pi$) of the two split modes as a function of the normalized transmission. The plot reveals a significant increase in $\kappa_0/2\pi$ with decreasing transmission depth, indicating the presence of parasitic coupling loss in the system. This loss can be attributed to the additional optical field decay into the surroundings caused by the tapered fiber [6]. Consequently, both the intrinsic and total linewidths vary depending on the coupling conditions. In the phonon laser experiment, a transmission depth of 0.17 results in a $\kappa_0/2\pi$ of 73 MHz and a total decay rate ($\kappa/2\pi$) of 103 MHz. For the strong coupling experiment, the transmission depth is set to approximately zero, yielding a $\kappa_0/2\pi$ of 95 MHz and a $\kappa/2\pi$ of 190 MHz. Moreover, the slight difference in $\kappa_0/2\pi$ between the two split modes can be attributed to their different optical field distributions.

Moreover, it is noteworthy that through improving the inductively coupled plasma (ICP) etching process, the yield of microresonators with intrinsic Q factors over 1×10^6 has increased to 100%, as shown in Fig. S5.

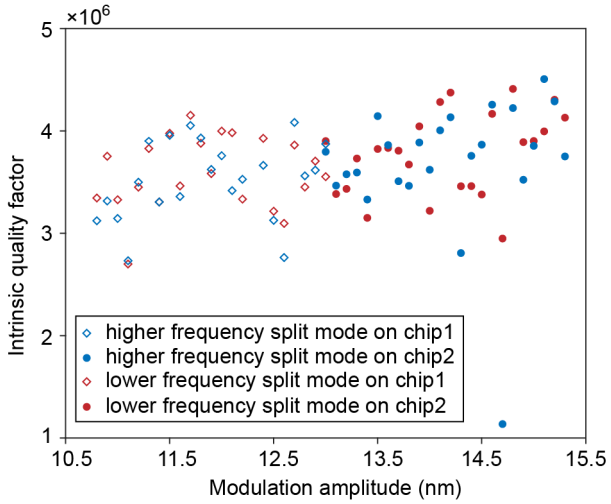

FIG. S5. **Intrinsic quality factors (Q_0) of the two split modes as a function of α for SiO_2 microresonators with a radius of $r_0 = 20$ μm, a thickness of $t = 1$ μm, and modulation period of $2m = 202$, respectively.**

S3. THEORETICAL MODEL FOR PHONON LASER GENERATION

In this section, we present a theoretical analysis of the phonon lasing in the SiO_2 microresonator system when the higher-frequency split mode is pumped. This scenario allows for the phonon lasing where the optical decay rate is larger than the phonon damping rate, i.e., $\kappa > \gamma_{\rm m}$.

Given that the modulation amplitude of the SiO_2 microresonator is much smaller than the optical wavelength, the dipole approximation can be applied to model the backscattering using Raleigh scattering theory. The total Hamiltonian of the system can be expressed as follows:

$$H_{\rm tot} = H_0 + H_{\rm back} + H_{\rm Bril} + H_{\rm vac} + H_{\rm dri} \tag{S9}$$

where H_0 represents the free Hamiltonian, $H_{\rm back}$ denotes the backscattering induced interaction Hamiltonian, $H_{\rm Bril}$ is the Brillouin scattering induced interaction Hamiltonian, $H_{\rm vac}$ is the additional dissipation resulting from coupling with the vacuum reservoir, and $H_{\rm dri}$ is the driving term. The angular frequencies of the optical and mechanical modes are represented by ω_0 and $\Omega_{\rm m}$, respectively. Due to the strong backscattering, the pump light will be backscattered into the counter-propagating direction, even though the SiO_2 microresonator is only pumped in one direction. Moreover, the Stokes light and acoustic waves are generated in both directions. The photon and phonon annihilation (creation) operators in both the CW and CCW directions for the optical mode a and mechanical mode b are defined as $a_{\rm cw}(a^\dagger_{\rm cw})$, $a_{\rm ccw}(a^\dagger_{\rm ccw})$, $b_{\rm cw}(b^\dagger_{\rm cw})$, and $b_{\rm ccw}(b^\dagger_{\rm ccw})$, respectively. The g_0 is the same for the Brillouin process in both directions, and we can then expand the Hamiltonian of the system as ($\hbar = 1$):

$$H_0 = \omega_0(a^\dagger_{\rm cw}a_{\rm cw} + a^\dagger_{\rm ccw}a_{\rm ccw}) + \Omega_{\rm m}(b^\dagger_{\rm cw}b_{\rm cw} + b^\dagger_{\rm cw}b_{\rm cw}) \tag{S10}$$

$$H_{\rm back} = \beta(a^\dagger_{\rm cw}a_{\rm cw} + a^\dagger_{\rm cw}a_{\rm ccw} + a^\dagger_{\rm ccw}a_{\rm ccw} + a^\dagger_{\rm ccw}a_{\rm cw}) \tag{S11}$$

$$H_{\rm Bril} = g_0(a^\dagger_{\rm cw}a_{\rm ccw}b_{\rm cw} + a_{\rm cw}a^\dagger_{\rm ccw}b^\dagger_{\rm cw} + a^\dagger_{\rm ccw}a_{\rm cw}b_{\rm ccw} + a_{\rm ccw}a^\dagger_{\rm cw}b^\dagger_{\rm ccw}) \tag{S12}$$

$$H_{\rm vac} = \sum \omega_{\rm j} d^\dagger_{\rm j} d_{\rm j} \tag{S13}$$

$$H_{\rm dri} = i(\varepsilon_{\rm d}a^\dagger_{\rm cw}e^{-i\omega_{\rm pump}t} + \varepsilon^*_{\rm d}a_{\rm cw}e^{i\omega_{\rm pump}t}) \tag{S14}$$

where β denotes the backscattering rate, which equals $\Delta f/2$. $d^\dagger_{\rm j}(d_{\rm j})$ represents the annihilation (creation) operator for photons with the angular frequency of $\omega_{\rm j}$ in the vacuum reservoir. The total energy decay rate for the optical mode a is defined as $\kappa = \kappa_0 + \kappa_1$, where κ_0 and κ_1 denote the intrinsic and external energy decay rates, respectively. The drive strength $\varepsilon_{\rm d} = \sqrt{\kappa_1 P_{\rm in}/\omega_{\rm pump}}$ quantifies the number of photons coupled into the SiO_2 microresonator per unit time, where $P_{\rm in}$ denotes the power of the pump light with the frequency of $\omega_{\rm pump}/2\pi$. The damping rate for the mechanical mode b is denoted as $\gamma_{\rm m}$.

Starting from the Hamiltonian of the system and utilizing the Bosonic commutation relations, we can simplify the Heisenberg equations of motion for the optical and mechanical modes in the rotating frame:

$$\dot{a}_{\rm cw} = (i(\Delta - \beta) - \frac{\kappa + \Gamma_{\rm R}}{2})a_{\rm cw} - (i\beta + \frac{\Gamma_{\rm R}}{2})a_{\rm ccw} - ig_0a_{\rm ccw}(b_{\rm cw} + b^\dagger_{\rm ccw}) + \varepsilon_d \tag{S15}$$

$$\dot{a}_{\rm ccw} = (i(\Delta - \beta) - \frac{\kappa + \Gamma_{\rm R}}{2}))a_{\rm ccw} - (i\beta + \frac{\Gamma_{\rm R}}{2})a_{\rm cw} - ig_0a_{\rm cw}(b_{\rm ccw} + b^\dagger_{\rm cw}) \tag{S16}$$

$$\dot{b}_{\rm cw} = (-i\Omega_{\rm m} - \frac{\gamma_{\rm m}}{2})b_{\rm cw} - ig_0a_{\rm cw}a^\dagger_{\rm ccw} \tag{S17}$$

$$\dot{b}_{\rm ccw} = (-i\Omega_{\rm m} - \frac{\gamma_{\rm m}}{2})b_{\rm ccw} - ig_0a_{\rm ccw}a^\dagger_{\rm cw} \tag{S18}$$

where $\Delta = \omega_{\rm pump} - \omega_+$ is the laser detuning from the cavity resonance, and $\Gamma_{\rm R}$ denotes the additional energy decay rate caused by the coupling into the vacuum reservoir [7].

The dynamic evolution of the optomechanical system is numerically analyzed utilizing the fourth-order Runge-Kutta method. To simplify the analysis without losing the underlying physics, we consider a special case where the pump light is on resonance with the optical mode, and the frequency splitting is equal to the mechanical frequency, resulting in $\Delta = 0$ and $\Delta f = 2\beta/2\pi = \Omega_{\rm m}/2\pi$. The intrinsic decay rate of the optical mode is fixed at $\kappa_0/2\pi$=80 MHz, and the external decay rate is varied with $\kappa_1/2\pi$ of 40 MH, 80 MHz, and 120 MHz for under-coupling (U.C.), critical-coupling (C.C), and over-coupling (O.C.) conditions, respectively. The damping rate for the mechanical mode is set at $\gamma_{\rm m}/2\pi = 60$ MHz. In this regime where the optical decay rate is larger than the phonon damping rate ($\kappa > \gamma_m$), the Brillouin lasing produces phonon linewidth narrowing [8], in contrast to Brillouin photon lasers in Refs. [9–11].

Figure S6 presents the transient evolution towards the steady state with a pump power of 100 mW under the critical-coupled condition. Figures S6(a) and S6(b) represent the intracavity photon numbers in the CW and CCW

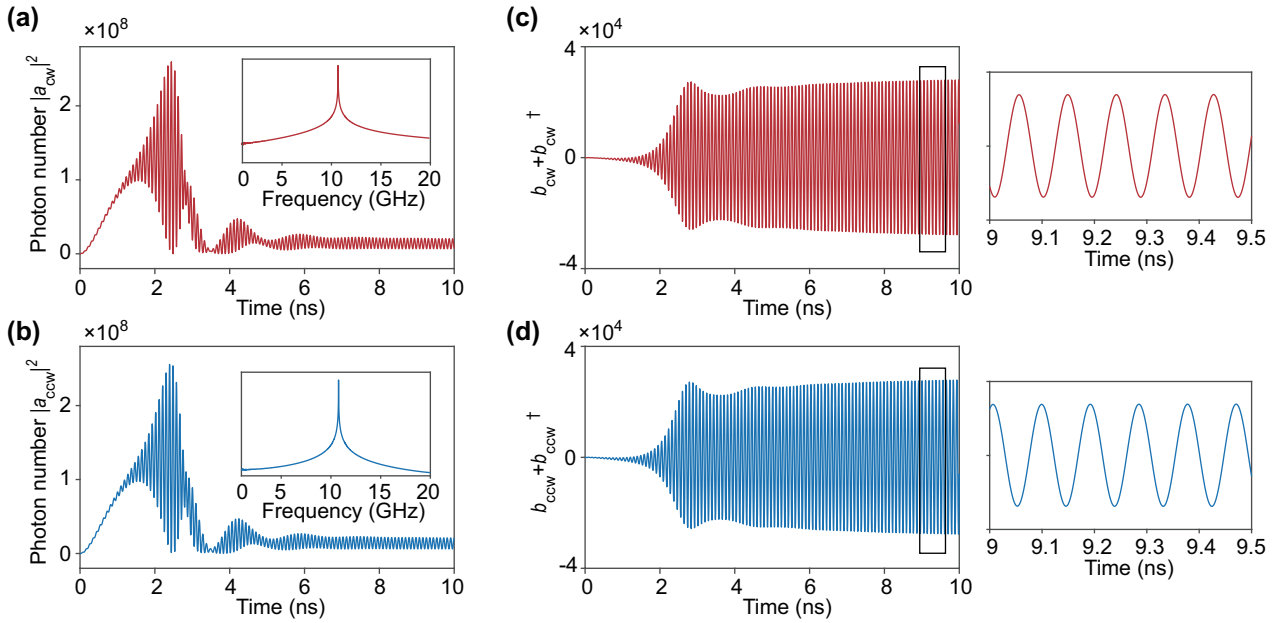

FIG. S6. **Transient evolution towards the steady state in the CW and CCW directions.** (a,b) Intracavity photon number evolution in the CW and CCW directions. Inset: Power spectrum density (PSD) of the intracavity photon number at the steady state, with the peak frequency corresponding to the mechanical frequency. (c,d) Transient evolution of mechanical displacement of the Brillouin phonon normalized to the x_{zpf} in the CW and CCW directions, oscillating at mechanical frequency. Inset: close-up of the normalized mechanical displacement.

directions, which initially increase and then damp to a steady-state oscillation. The oscillation frequency corresponds to the mechanical frequency ($\Omega_{\mathrm{m}}/2\pi$), as illustrated in the power spectral densities of the intracavity photon numbers, in the insets of Figs. S6(a) and S6(b). Even though the pump light is only coupled to the cavity in the CW direction, the intracavity photon number in the CCW direction is comparable to that in the CW direction, due to the strong backscattering. Moreover, the Brillouin phonons are generated in both directions through a combination of the electrostriction and photoelastic effects. Figures S4(c) and S4(d) represent the mechanical displacement of the Brillouin phonon normalized to the x_{zpf} in the CW and CCW directions, respectively. At the steady state, the mechanical displacement also oscillates at the mechanical frequency $\Omega_{\mathrm{m}}/2\pi$, as revealed by the close-up of the displacement.

We also present an analysis of the steady-state phonon number (N) for various pump powers. Figure S7(a) shows the N in both the CW and CCW directions at a critical-coupling condition as a function of pump power. Below the threshold power, N fluctuates around thermal phonon number $n_{\mathrm{th}} = k_{\mathrm{B}}T/\hbar\Omega_{\mathrm{m}} \approx 610$, where k_{B} is the Boltzmann constant and T is the temperature. Above the threshold power, N increases dramatically. The approximately equal number of pump photons in the CW and CCW directions leads to nearly the same number of phonons in the two directions. In the regime where the optical decay rate is larger than the phonon damping rate ($\kappa > \gamma_m$), the phonon linewidth ($\Delta\nu$) can be expressed as [8]:

$$\Delta\nu = \Delta\nu_{\mathrm{th}} + \frac{\Delta\nu_{\mathrm{p}}}{(1+\kappa/\gamma_{\mathrm{m}})^2} \tag{S19}$$

$$\Delta\nu_{\mathrm{th}} = \frac{\gamma_{\mathrm{m}} n_{\mathrm{th}}}{4\pi N} \tag{S20}$$

where $\Delta\nu_{\mathrm{th}}$ represents the linewidth originating from the thermal noise (Schawlow-Townes linewidth), while the second term on the right side of Eq. S19 is attributed to the linewidth of the pump laser ($\Delta\nu_{\mathrm{p}}$), which is narrowed by a factor of $(1+\kappa/\gamma_{\mathrm{m}})^2$. The linewidth from the pump laser can reach a very low level by using a narrow linewidth pump laser. For instance, by using a fiber laser with a typical linewidth of approximately 10 Hz, the linewidth attributed from the pump laser can be decreased to below 1 Hz for a critical-coupling condition. Therefore, we only consider the linewidth that originates from the thermal noise in the following simulation. As the pump power increases, N increases, leading to a decrease in the Schawlow-Townes linewidth. Figure S7(b) plots the Schawlow-Townes linewidth in both the CW and CCW directions as a function of pump power at a critical-coupling condition. Below the threshold power, $\Delta\nu_{\mathrm{th}}$ fluctuates around 60 MHz, which corresponds to the intrinsic linewidth of the mechanical mode at an

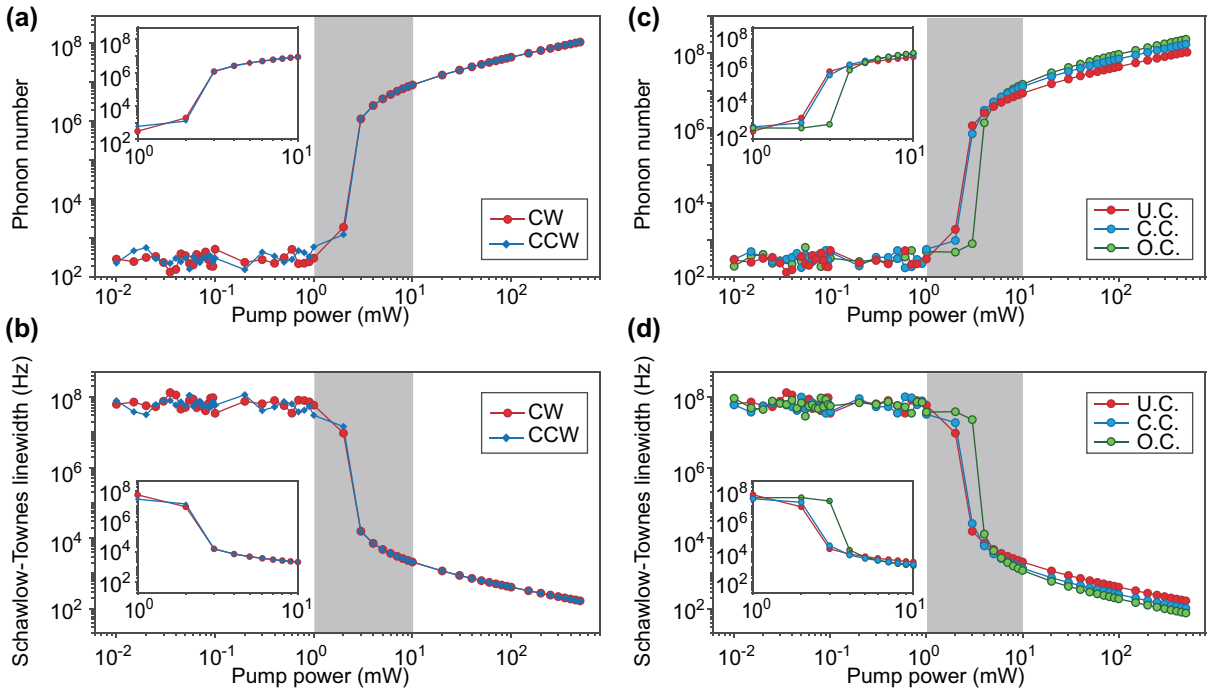

FIG. S7. **Phonon number and Schawlow-Townes linewidth in the CW and CCW directions.** (a,b) Phonon number and Schawlow-Townes linewidth in the CW and CCW directions at the critical-coupling condition as a function of the pump power. (c,d) Phonon number and Schawlow-Townes linewidth in the CW directions, as a function of the pump power, with $\kappa_0/2\pi$=80 MHz, and $\kappa_1/2\pi$=40 MHz, 80 MHz, 120 MHz, respectively. The red, blue, and green dots represent the results for the under-coupled, critical-coupled, and over-coupled conditions. The insets show the zoom-ins with the optical power in the range of 1-10 mW.

ambient temperature. Above the threshold power, the Schawlow-Townes linewidth decreases dramatically due to the significantly increased phonon number. The coupling conditions also affect the intracavity phonon numbers and thus the Schawlow-Townes linewidth. Figures S7(c) and S7(d) plot the phonon numbers and Schawlow-Townes linewidths for different coupling conditions. Due to the equal phonon numbers in the CW and CCW directions, we only plot the results for the CW direction. Our results indicate that the threshold power increases with the increase of the total optical decay rate, but the phonon number increases more rapidly when the pump power exceeds the threshold power under the over-coupled condition, thereby enabling a narrower Schawlow-Townes linewidth.

S4. EXPERIMENTAL DETAILS FOR PHONON LASER GENERATION AND MEASUREMENT

This section provides experimental details of the phonon lasing and measurement. We first measure the short-term linewidth of the pump laser using the self-heterodyne technique described in Ref. [12, 13], as elaborated on in the Methods section in the main text. As illustrated in Fig. S8(a), the laser under test is divided into two channels using a 50:50 beam splitter. One of the channels is shifted by 55 MHz in frequency using an acousto-optic modulator (AOM), while the other passes through a 5-km-long fiber delay to form a modified Mach-Zehnder interferometer (MZI). The two channels are then recombined, and the resulting beat note signal is detected by a photodetector (PD) and monitored by an oscilloscope with a sampling rate of 625 MHz. By performing a Hilbert transform (HT), phase fluctuations of the laser can be extracted, as illustrated in Fig. S8(b). The single-sideband (SSB) frequency noise is obtained by applying a fast-Fourier-transform (FFT), as shown in Fig. S8(c). According to the noise theory, the contribution of white noise is independent of frequency offset, and the linewidth of the Lorentzian spectral lineshape can be obtained by multiplying the white-noise SSB frequency noise by 2π [14]. The white noise level of the pump laser we used in the experiment is measured to be 44.114 $\mathrm{Hz^2Hz^{-1}}$, corresponding to a short-term linewidth of 277.18 Hz.

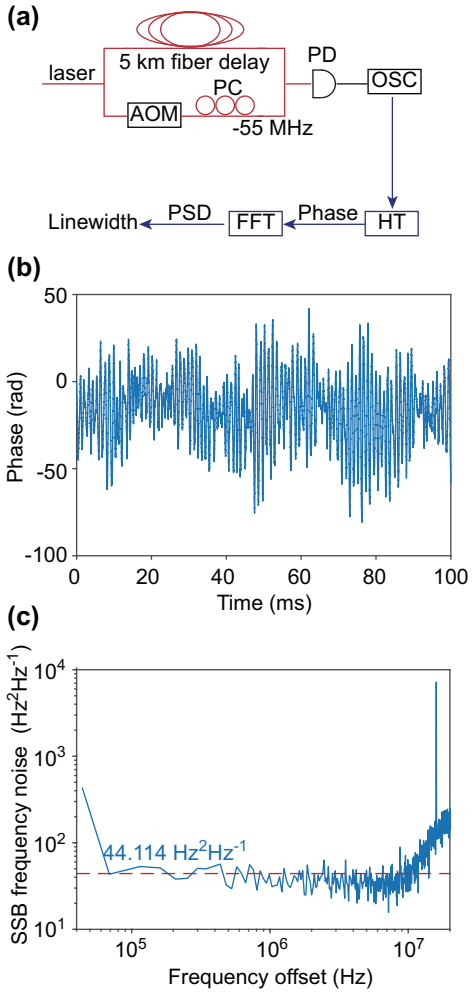

FIG. S8. **Short-term linewidth measurement of the pump laser.** (a) Schematic of the self-heterodyne measurement setup. AOM: acousto-optic modulator; PC: polarization controller; PD: photodetector; OSC: oscilloscope; HT: Hilbert transform; FFT: fast-Fourier-transform; PSD: power spectra density. (b) Phase evolution of the pump laser in the time domain; (c) SSB frequency noise of the pump laser, revealing a short-term linewidth of the pump laser is 277.18 Hz.

The experimental setup for phonon lasing and measurement is presented in Fig. S9(a). A tunable continuous-wave (c.w.) laser is amplified using an erbium-doped fiber amplifier (EDFA) and then coupled into the SiO_2 microresonator via a tapered fiber. The transmitted light from the SiO_2 microresonator, including both the pump and Stokes light, is split into three channels. The first channel is detected by a photodetector and the transmission spectrum of the SiO_2 microresonator is measured by an oscilloscope. The second channel is detected by another photodetector and

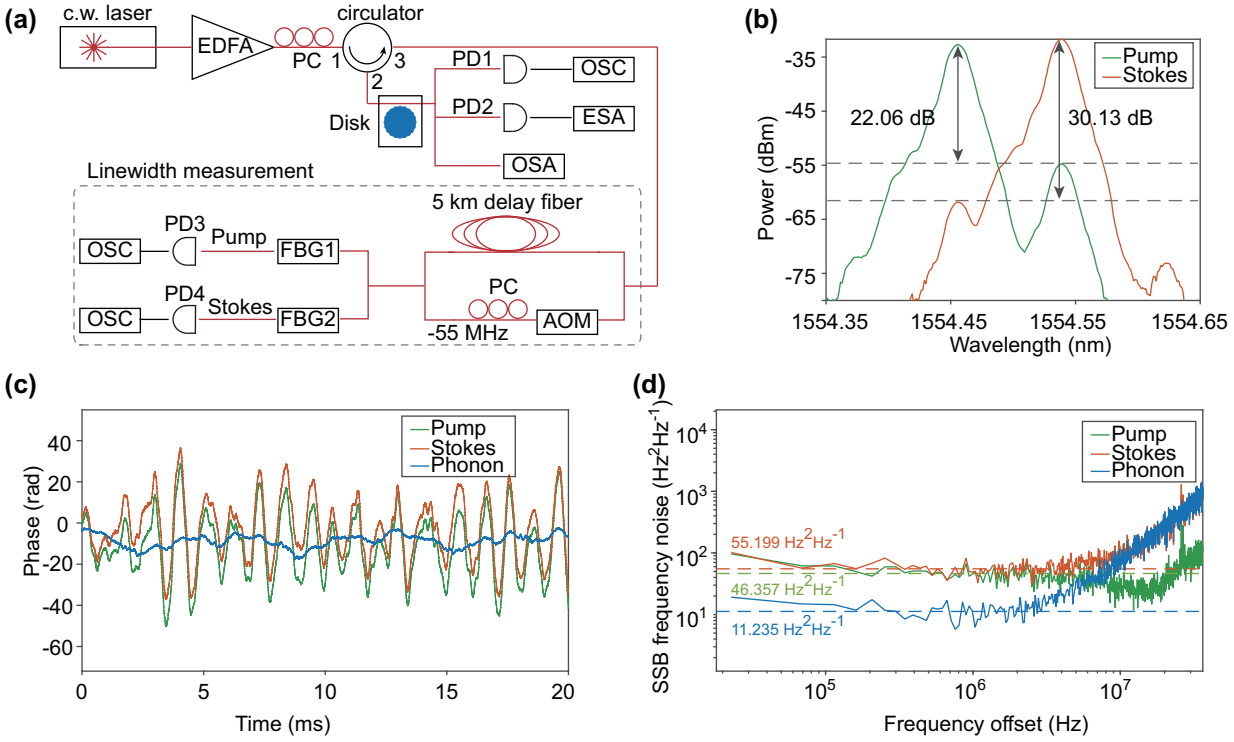

FIG. S9. **Phonon lasing measurement.** (a) Experimental setup for the phonon lasing measurement. EDFA: erbium-doped fiber amplifier; PC: polarization controller; PD: photodetector; OSA: optical spectrum analyzer; OSC: oscilloscope; ESA: electrical spectrum analyzer; AOM: acousto-optic modulator; FBG: fiber Bragg grating. (b) Optical spectra for the pump (green curve) and Stokes (red curve) light with power ratios of 22.06 dB and 30.13 dB, respectively. (c) Phase evolutions of the pump laser, Stokes laser, and phonon laser, respectively. (d) SSB frequency noise for the pump laser, Stokes laser, and phonon laser, showing linewidths of 291.27 Hz, 346.82 Hz, and 70.59 Hz, respectively.

measured by an electronic spectrum analyzer (ESA) to obtain the phonon laser spectrum. The third channel is directed to an OSA to obtain the SBS spectrum. Starting from the blue-detuned side of the higher-frequency split mode, the wavelength of the pump laser is gradually scanned up. The phonon laser linewidth is measured by analyzing the backscattered pump and Stokes light from the SiO_2 microresonator, using the technique mentioned above.

To measure the linewidth of the phonon laser, we employ a setup consisting of two tunable fiber Bragg gratings (FBGs) to filter out the pump and Stokes light, respectively, enabling the separate measurement of their linewidths. The power ratios between them are maintained at more than 20 dB, as shown in Fig. S9(b). The output light is then detected by two photodetectors and recorded by an oscilloscope. The phase difference between the pump and Stokes light is extracted as the phase evolution of the phonon laser, as presented in Fig. S9(c). The short-term linewidths of the pump, Stokes, and phonon lasers can then be obtained using the method mentioned above. The SSB frequency noise of the pump, Stokes, and phonon lasers are presented in the green, red, and blue curves in Fig. S9(d), respectively. As the system is in the regime where the optical decay rate is larger than the phonon damping rate ($\kappa > \gamma_m$), the phonon linewidth is significantly reduced to 70.59 Hz, whereas the linewidth of the Stokes laser remains similar to that of the pump laser. According to the theoretical result obtained using Eq. S19, the lowest achievable phonon linewidth is approximately 35 Hz, which is the linewidth contributed by the pump laser.

It is noteworthy that third-harmonic generation (THG) was observed in the optomechanical strong coupling experiment when the pump power was increased to around 800 mW, resulting in the emission of green light, as shown in Fig. S10.

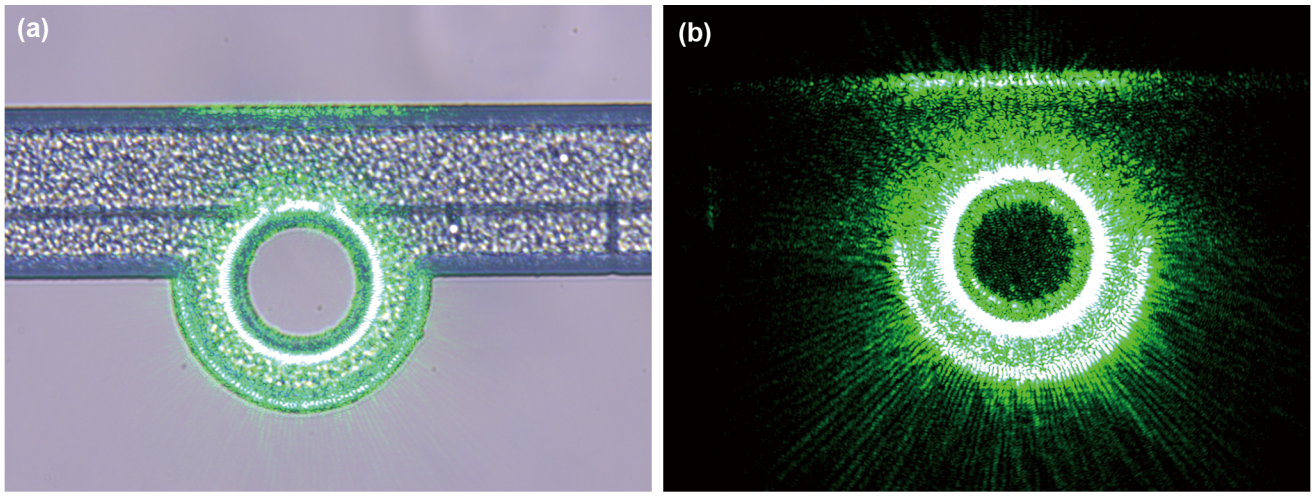

FIG. S10. **Optical microscope images of the microresonator with THG occurred when the illumination light is on (a), and off (b).**

S5. THEORETICAL MODEL FOR STRONG COUPLING

In this section, we present a comprehensive theoretical analysis of the optomechanical strong coupling in the SiO_2 microresonator system. When a pump laser is used to drive the lower-frequency split mode, a significant intracavity optical field is generated, which then interacts with the mechanical mode, leading to resonant scattering of the anti-Stokes light into the higher-frequency split mode. Therefore, the Hamiltonian of the Brillouin interaction term can be rewritten as ($\hbar = 1$):

$$H_{\mathrm{Bril}} = g_0(a_{\mathrm{cw}}^{\dagger}a_{\mathrm{ccw}}b_{\mathrm{cw}}^{\dagger} + a_{\mathrm{cw}}^{\dagger}a_{\mathrm{ccw}}b_{\mathrm{ccw}} + a_{\mathrm{ccw}}^{\dagger}a_{\mathrm{cw}}b_{\mathrm{ccw}}^{\dagger} + a_{\mathrm{ccw}}^{\dagger}a_{\mathrm{cw}}b_{\mathrm{cw}}) \tag{S21}$$

To linearize the Hamiltonian, we apply the transformation $a_{\mathrm{cw,ccw}} \to a_{\mathrm{cw,ccw}} + \alpha_{\mathrm{cw,ccw}}$, where $\alpha_{\mathrm{cw,ccw}}$ and $a_{\mathrm{cw,ccw}}$ represent the intracavity steady (perturbed) optical field amplitudes in the CW and CCW directions, respectively. Under the rotation approximation, the resulting linearized Hamiltonian in the rotating frame can be expressed in matrix form with the eigenvector of $[a_{\mathrm{cw}}, a_{\mathrm{ccw}}, b_{\mathrm{cw}}, b_{\mathrm{ccw}}]^T$, as follows:

$$H_{\mathrm{new}} = \begin{bmatrix} -\Delta + g - i\frac{\kappa}{2} & g + i\frac{\Gamma_{\mathrm{R}}}{2} & G_2 & 0 \\ g + i\frac{\Gamma_{\mathrm{R}}}{2} & -\Delta + g - i\frac{\kappa}{2} & 0 & G_1 \\ G_2^{\star} & 0 & \Omega_{\mathrm{m}} - i\frac{\gamma_{\mathrm{m}}}{2} & 0 \\ 0 & G_1^{\star} & 0 & \Omega_{\mathrm{m}} - i\frac{\gamma_{\mathrm{m}}}{2} \end{bmatrix} \tag{S22}$$

where $\Delta = \omega_{\mathrm{pump}} - \omega_{-}$ is the laser detuning from the cavity resonance, $G_{1,2} = g_0 \times \alpha_{\mathrm{cw,ccw}}$ is the cavity-enhanced optomechanical coupling rate in the CW (CCW) direction.

We first examine them under some specific conditions. To simplify the analysis, we set $\Delta = 0$, $\Omega_{\mathrm{m}} = 2g$, and $\Gamma_{\mathrm{R}} = 0$. In addition, we first consider the scenario where the cavity-enhanced coupling rate is absent, $G_1 = G_2 = G_1^{\star} = G_2^{\star} = 0$. Under these conditions, the eigenvectors and eigenvalues can be determined as:

$$V = \begin{bmatrix} 0 & -1 & 1 & 0 \\ 0 & 1 & 1 & 0 \\ 1 & 0 & 0 & 0 \\ 0 & 0 & 0 & 1 \end{bmatrix}; E = \begin{bmatrix} 2g - i\frac{\gamma_{\mathrm{m}}}{2} \\ -i\frac{\kappa}{2} \\ 2g - i\frac{\kappa}{2} \\ 2g - i\frac{\gamma_{\mathrm{m}}}{2} \end{bmatrix} \tag{S23}$$

It can be observed that the first and fourth columns of the eigenvectors represent the CW and CCW mechanical modes, while the second and third columns correspond to the anti-symmetric and symmetric standing-wave optical modes resulting from the strong backscattering, with eigenvalues of $-i\frac{\kappa}{2}$ and $2g - i\frac{\kappa}{2}$ in the rotating frame, respectively.

When cavity-enhanced optomechanical coupling rate $G_1 = G_2 = G_1^{\star} = G_2^{\star} = G$ is considered, the eigenvectors and eigenvalues are given as follows:

$$V = \begin{bmatrix} A & B & C & D \\ F & G & H & I \\ -1 & -1 & 1 & 1 \\ 1 & 1 & 1 & 1 \end{bmatrix}; E = \begin{bmatrix} g - i\frac{\gamma_m+\kappa}{4} + \sqrt{\frac{(4G-4ig-\gamma_m+\kappa)\times(4G+4ig+\gamma_m-\kappa)}{16}} \\ g - i\frac{\gamma_m+\kappa}{4} - \sqrt{\frac{(4G-4ig-\gamma_m+\kappa)\times(4G+4ig+\gamma_m-\kappa)}{16}} \\ 2g - i\frac{\gamma_m+\kappa}{4} - \sqrt{\frac{(4G-\gamma_m+\kappa)\times(4G+\gamma_m-\kappa)}{16}} \\ 2g - i\frac{\gamma_m+\kappa}{4} + \sqrt{\frac{(4G-\gamma_m+\kappa)\times(4G+\gamma_m-\kappa)}{16}} \end{bmatrix} \tag{S24}$$

where

$$A = \frac{-4g + i(\kappa+\gamma_m) - \sqrt{(4G+\gamma_m+i4g-\kappa)(4G-\gamma_m-i4g+\kappa)}}{4G} + \frac{4g-i\gamma_m}{2G}$$
$$B = \frac{-4g + i(\kappa+\gamma_m) + \sqrt{(4G+\gamma_m+i4g-\kappa)(4G-\gamma_m-i4g+\kappa)}}{4G} + \frac{4g-i\gamma_m}{2G}$$
$$C = \frac{8g - i(\kappa+\gamma_m) - \sqrt{(4G+\gamma_m-\kappa)(4G-\gamma_m+\kappa)}}{4G} - \frac{4g-i\gamma_m}{2G}$$
$$D = \frac{8g - i(\kappa+\gamma_m) + \sqrt{(4G+\gamma_m-\kappa)(4G-\gamma_m+\kappa)}}{4G} - \frac{4g-i\gamma_m}{2G}$$
$$F = \frac{4g - i(\kappa+\gamma_m) + \sqrt{(4G+\gamma_m+i4g-\kappa)(4G-\gamma_m-i4g+\kappa)}}{4G} - \frac{4g-i\gamma_m}{2G}$$
$$G = \frac{4g - i(\kappa+\gamma_m) - \sqrt{(4G+\gamma_m+i4g-\kappa)(4G-\gamma_m-i4g+\kappa)}}{4G} - \frac{4g-i\gamma_m}{2G}$$
$$H = \frac{8g - i(\kappa+\gamma_m) - \sqrt{(4G+\gamma_m-\kappa)(4G-\gamma_m+\kappa)}}{4G} - \frac{4g-i\gamma_m}{2G}$$
$$I = \frac{8g - i(\kappa+\gamma_m) + \sqrt{(4G+\gamma_m-\kappa)(4G-\gamma_m+\kappa)}}{4G} - \frac{4g-i\gamma_m}{2G}$$

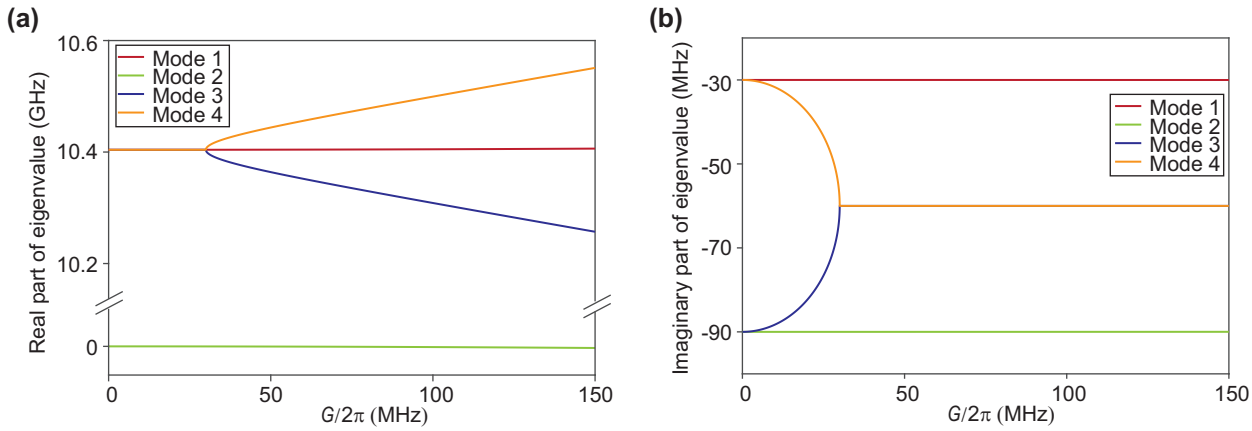

FIG. S11. **Eigenvalues of the linearized Hamiltonian of the optomechanical system.** (a) Real part and (b) Imaginary part of eigenvalues versus cavity-enhanced coupling rate ($G/2\pi$). The parameters used are $\kappa/2\pi$=180 MHz, $\gamma_m/2\pi$=60 MHz, and $2g = \Omega_m = 2\pi\times10.404$ GHz.

In the SiO_2 microresonator system, the optomechanical interaction gives rise to four hybridized modes, designated as modes 1-4 in the eigenvectors of Eq. S24. The real part of the eigenvalues indicates the resonance frequency of each mode, while the imaginary part represents the total amplitude decay rate. The dependence of the real and imaginary parts of the eigenvalues on the $G/2\pi$ is plotted in Fig. S11. When $G/2\pi$ is lower than the threshold value of $G_{th}/2\pi = \frac{\kappa-\gamma_m}{4\cdot2\pi}$, the frequencies of modes 1, 3, 4 are degenerate, whereas a frequency splitting occurs between modes 3 and 4 when $G > G_{th}$. Moreover, the amplitude decay rates of modes 3 and 4 converge to $\frac{\kappa+\gamma_m}{4\cdot2\pi}$ at G_{th} and remain constant when $G > G_{th}$. Thus the eigenvalues change character at the threshold where the root changes from purely imaginary to real-valued. This corresponds to the transition into the strong-coupling regime. The normal-mode splitting formally occurs as soon as $G > G_{th}$, but it is not resolvable until $\sqrt{\frac{(4G-\gamma_m+\kappa)\times(4G+\gamma_m-\kappa)}{16}}$ exceeds the

Table S1 | Key parameters for the single mechanical mode simulation.

P_d (mW)	$2g/2\pi$ (GHz)	$g_0/2\pi$ (kHz)	$\kappa_0/2\pi$ (MHz)	$\kappa_1/2\pi$ (MHz)	$\Omega_m/2\pi$ (GHz)	$\gamma_m/2\pi$ (MHz)
500	10.404	12.52	90	90	10.167	60

TABLE S1. Key parameters used in the optomechanical strong coupling simulation for the single mechanical mode scenario.

effective decay rate of the hybrid optical-mechanical modes $\frac{\kappa+\gamma_m}{4\cdot 2\pi}$. Therefore, well-resolved mode splitting requires a stronger condition of $G > \sqrt{(\kappa^2+\gamma_m^2)/8}$. When the coupling rate reaches this condition, the two splitting peaks become resolvable, and also correspond to the occurrence of Rabi oscillations in the time domain.

We experimentally determine whether strong coupling occurs by measuring the reflection spectrum of the SiO_2 microresonator. To achieve this, a probe term with $H_p = i\epsilon_p(a_{cw}^\dagger e^{-i(\omega_{probe}-\omega_{pump})t} - a_{cw}e^{i(\omega_{probe}-\omega_{pump})t})$ is introduced into the Hamiltonian. Here, ϵ_p represents the strength of the probe light, defined as $\sqrt{\frac{\kappa_1 P_p}{\omega_{probe}}}$, where P_p and ω_{probe} are the power and angular frequency of the probe light, respectively. The probe light is detuned by δ from the pump laser. In the rotating frame, the Heisenberg equations of motion can be expressed as:

$$\frac{d}{dt}\begin{bmatrix} a_{cw} \\ a_{ccw} \\ b_{cw} \\ b_{ccw} \end{bmatrix} = -i \begin{bmatrix} mm & gg & G_2 & 0 \\ gg & mm & 0 & G_1 \\ G_2^\star & 0 & nn & 0 \\ 0 & G_1^\star & 0 & nn \end{bmatrix} \begin{bmatrix} a_{cw} \\ a_{ccw} \\ b_{cw} \\ b_{ccw} \end{bmatrix} - \begin{bmatrix} \epsilon_p a_{cw} \\ 0 \\ 0 \\ 0 \end{bmatrix} \tag{S25}$$

where $\delta = \omega_{probe} - \omega_{pump}$ is the frequency detuning between the probe and pump lasers. To simplify notation, we define $mm = -\Delta - \delta + g - i\frac{\kappa}{2}$, $gg = g + i\frac{\Gamma_R}{2}$, and $nn = \Omega_m - i\frac{\gamma_m}{2}$.

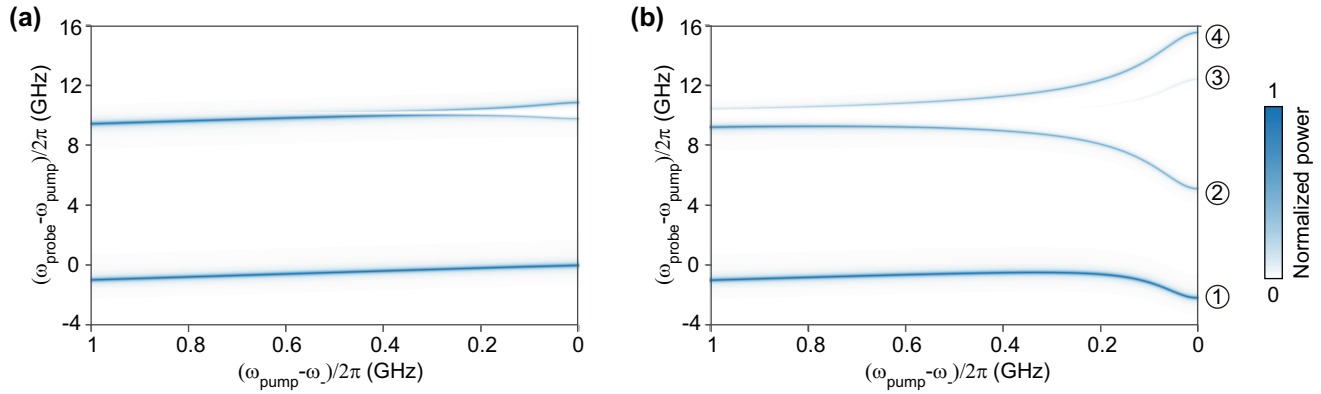

FIG. S12. **Simulated spectra of the optomechanical strong coupling in the single mechanical mode scenario.** (a) Theoretically predicted spectrum using parameters in Table S1. (b) Theoretically predicted spectrum with $g_0/2\pi$ of 125.2 kHz.

The steady-state solutions of the Heisenberg equations of motion are presented in Fig. S12, using the parameters listed in Table S1. As the SiO_2 microresonator system possesses four non-degenerate eigenvalues, the steady-state spectrum is expected to exhibit four non-degenerate peaks. However, in Fig. S12(a), only three peaks are clearly visible. To further investigate this phenomenon, we artificially increase the value of $g_0/2\pi$ by a factor of 10 to 125.2 kHz, and the corresponding spectrum is shown in Fig. S12(b), where a new, weak peak appears, confirming the existence of four non-degenerate modes in the SiO_2 microresonator system. The four modes are labeled as modes 1 to 4 in order of increasing frequency. Peak 1 corresponds to the lower-frequency split mode, and a resolvable anti-crossing occurs between modes 2 and 4 when $G > \frac{\kappa+\gamma_m}{4}$. Mode 3 is too weak to be experimentally detected.

S6. EXPERIMENTAL DETAILS FOR STRONG COUPLING

The experimental setup for measuring the optomechanical strong coupling is illustrated in Fig. S13. A c.w. laser is used to pump the lower-frequency split mode, and its frequency ω_{pump} is thermally locked to the cavity resonance with a detuning of $\omega_{\mathrm{pump}} - \omega_{-}$. The transmission spectrum around the pump mode of the SiO_2 microresonator is detected by a photodetector and monitored by an oscilloscope, while the reflected light from the SiO_2 microresonator is detected by another photodetector. An electro-optic modulator (EOM) is employed to modulate the pump light, with its modulation frequency being scanned using a vector network analyzer (VNA). When the probe light is resonant with the higher-frequency split mode a_{+}, both the pump and probe light can couple into and out of the SiO_2 microresonator, generating a beat note signal at a frequency of $\omega_{\mathrm{probe}} - \omega_{\mathrm{pump}}$ that can be measured in the optical response spectrum S_{21} by the VNA.

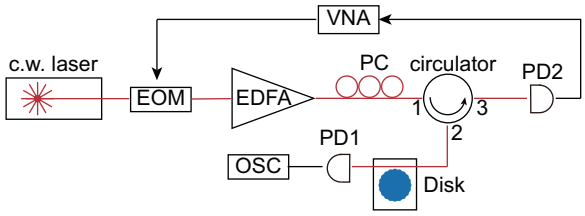

FIG. S13. **Experimental setup for optomechanical strong coupling.** EOM: electro-optic modulator; VNA: vector network analyzer.

[1] G. S. Wiederhecker, P. Dainese, and T. P. Mayer Alegre, Brillouin optomechanics in nanophotonic structures, APL photonics **4**, 071101 (2019).

[2] Y. A. Espinel, F. G. Santos, G. O. Luiz, T. M. Alegre, and G. S. Wiederhecker, Brillouin optomechanics in coupled silicon microcavities, Sci. Rep. **7**, 43423 (2017).

[3] P. T. Rakich, C. Reinke, R. Camacho, P. Davids, and Z. Wang, Giant enhancement of stimulated brillouin scattering in the subwavelength limit, Phys. Rev. X **2**, 011008 (2012).

[4] R. Van Laer, R. Baets, and D. Van Thourhout, Unifying Brillouin scattering and cavity optomechanics, Phys. Rev. A **93**, 053828 (2016).

[5] T. J. Kippenberg, S. M. Spillane, B. Min, and K. J. Vahala, Theoretical and experimental study of stimulated and cascaded Raman scattering in ultrahigh-Q optical microcavities, IEEE Journal of selected topics in Quantum Electronics **10**, 1219 (2004).

[6] S. Spillane, T. Kippenberg, O. Painter, and K. Vahala, Ideality in a fiber-taper-coupled microresonator system for application to cavity quantum electrodynamics, Phys. Rev. Lett. **91**, 043902 (2003).

[7] J. Zhu, S. K. Ozdemir, Y.-F. Xiao, L. Li, L. He, D.-R. Chen, and L. Yang, On-chip single nanoparticle detection and sizing by mode splitting in an ultrahigh-q microresonator, Nat. photon. **4**, 46 (2010).

[8] J. Xiong, Z. Huang, K. Cui, X. Feng, F. Liu, W. Zhang, and Y. Huang, Phonon and photon lasing dynamics in optomechanical cavities, Fundam. Res. **3**, 37 (2023).

[9] J. Li, H. Lee, T. Chen, and K. J. Vahala, Characterization of a high coherence, brillouin microcavity laser on silicon, Opt. Express **20**, 20170 (2012).

[10] H. Lee, T. Chen, J. Li, K. Y. Yang, S. Jeon, O. Painter, and K. J. Vahala, Chemically etched ultrahigh-q wedge-resonator on a silicon chip, Nat. Photon. **6**, 369 (2012).

[11] S. Gundavarapu, G. M. Brodnik, M. Puckett, T. Huffman, D. Bose, R. Behunin, J. Wu, T. Qiu, C. Pinho, N. Chauhan, *et al.*, Sub-hertz fundamental linewidth photonic integrated brillouin laser, Nat. Photon. **13**, 60 (2019).

[12] Z. Yuan, H. Wang, P. Liu, B. Li, B. Shen, M. Gao, L. Chang, W. Jin, A. Feshali, M. Paniccia, *et al.*, Correlated self-heterodyne method for ultra-low-noise laser linewidth measurements, Opt. Express **30**, 25147 (2022).

[13] C. Lao, X. Jin, L. Chang, H. Wang, Z. Lv, W. Xie, H. Shu, X. Wang, J. E. Bowers, and Q.-F. Yang, Quantum decoherence of dark pulses in optical microresonators, Nat. Commun. **14**, 1802 (2023).

[14] G. Di Domenico, S. Schilt, and P. Thomann, Simple approach to the relation between laser frequency noise and laser line shape, Appl. Opt. **49**, 4801 (2010).